Yang Xu
Daniel J. Epstein Department of Industrial and Systems Engineering,
University of Southern California,
Los Angeles, CA 90089
e-mail: yxu195@usc.edu

Yizhen Zhu
Department of Aerospace and Mechanical Engineering,
University of Southern California,
Los Angeles, CA 90089
e-mail: yizhenzh@usc.edu

Yifeng Sun
Department of Aerospace and Mechanical Engineering,
University of Southern California,
Los Angeles, CA 90089
e-mail: yifengsu@usc.edu

Jie Jin
Daniel J. Epstein Department of Industrial and Systems Engineering,
University of Southern California,
Los Angeles, CA 90089
e-mail: jiejin@usc.edu

Yong Chen[1]
Professor
Daniel J. Epstein Department of Industrial and Systems Engineering,
University of Southern California,
Los Angeles, CA 90089;
Department of Aerospace and Mechanical Engineering,
University of Southern California,
Los Angeles, CA 90089
e-mail: yongchen@usc.edu

A Vibration-Assisted Separation Method for Constrained-Surface-Based Stereolithography

For the bottom-up based stereolithography (SL) process, a separation process is required to detach the newly cured layer from the constrained surface in the fabrication process. Excessive separation force will cause damage to the built layers and the constrained surface. Different surface coatings, platform motions including tilting and sliding, and the utilization of oxygen-permeable films have been developed to address the separation-related problems. Among these approaches, the vibration-assisted (VA) separation method to reduce the separation force has limited study. The underlying mechanism of the VA separation-based method remains unexplored, and the best way to use VA separation in the bottom-up based SL process is still unclear. In this paper, a new VA separation design for the SL process is presented. A prototype system was built to study the VA separation mechanism. Experiments on the separation performance under different parameters, including vibration frequency, pre-stress level, and exposure area, were conducted. Based on the collected separation force data, an analytical model based on the mechanics of fatigue fracture was built. The separation behaviors related to different shape size and topology were also studied and compared. The results showed that the separation force in SL was significantly reduced using the VA separation-based method. Furthermore, the relationship between the separation force and the separation time conforms to the stress-based fatigue model. This study also provides insights on how to choose process parameters by considering the trade-offs between separation force and building efficiency. [DOI: 10.1115/1.4048445]

Keywords: additive manufacturing, stereolithography, vat photopolymerization, vibration, constrained surface, modeling and simulation

1 Introduction

Stereolithography (a.k.a. vat photopolymerization) is an additive manufacturing (AM) technology that utilizes the photopolymerization process to fabricate a three-dimensional (3D) object layer by layer. It is one of the most popular AM processes, which has been widely used in various applications [1,2]. Compared with other polymer-based AM processes such as extrusion or jetting processes, stereolithography (SL) can fabricate objects with high accuracy, resolution, and surface quality [3–5]. In the SL process, an irradiation light source such as a digital light processing (DLP) projector or a scanning laser beam is used to cure the liquid resin in the vat [6,7]. In general, there are two approaches in photocuring liquid resin, i.e., the free surface method and the constrained-surface method (Fig. 1).

In the free surface method, the liquid resin is exposed to light and solidified with no constrained surface, and then a new layer of liquid resin is refilled by lowering the building platform down. In comparison, in the constrained-surface method, there are two kinds of configurations, top-down and bottom-up (see Figs. 1(*a*)–1(*c*)) [8,9]. In both configurations, liquid resin is sandwiched between the built layers and the constrained surface. The light penetrates through the transparent constrained surface and cures the liquid resin. The constrained-surface method has several advantages over the free surface method. For example, (1) a much smaller layer thickness can be achieved because the gap size is only determined by the *Z* stage resolution regardless of the fluidic properties of the liquid resin. (2) A flat layer of the new liquid polymer could be refilled in a short time, even if the liquid is viscous [10]. (3) The building velocity is faster since the oxygen inhibition effect in the free surface method is eliminated [11]. (4) Further, in the bottom-up constrained-surface method, the part height is no longer limited by the resin vat depth; thus, a shallow vat can be used to reduce the required volume of the liquid resin [12].

Despite the aforementioned advantages of the constrained-surface-based SL process, there exists a bottleneck that needs to be addressed. That is, the curing process leads to adhesive bonding between the newly cured layer and the constrained surface. In order to proceed with the fabrication process, a separation force is required to detach them [13]. Most industrial bottom-up SL uses direct pulling-up as the separation method (Figs. 2(*a*)–2(*c*)). However, during the pulling-up stage, the newly cured layer of a large area may fail to be raised; instead, it may attach to the bottom surface, and the building process will fail [15]. Moreover, the excessive separation force may damage the constrained surface during the recursive separation process. Such a large separation force limits the printable layer area and the reliability of the 3D printing process. So far, all the commercial SL machines with large

[1]Corresponding author.

Manuscript received May 18, 2020; final manuscript received May 29, 2020; published online November 11, 2020. Assoc. Editor: Y. Lawrence Yao.

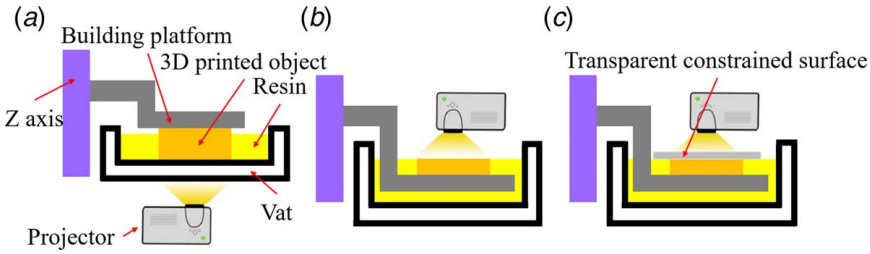

Fig. 1 Photocuring configurations of the SL process: (*a*) bottom-up constrained-surface configuration, (*b*) top-down free-surface configuration, and (*c*) top-down constrained-surface configuration

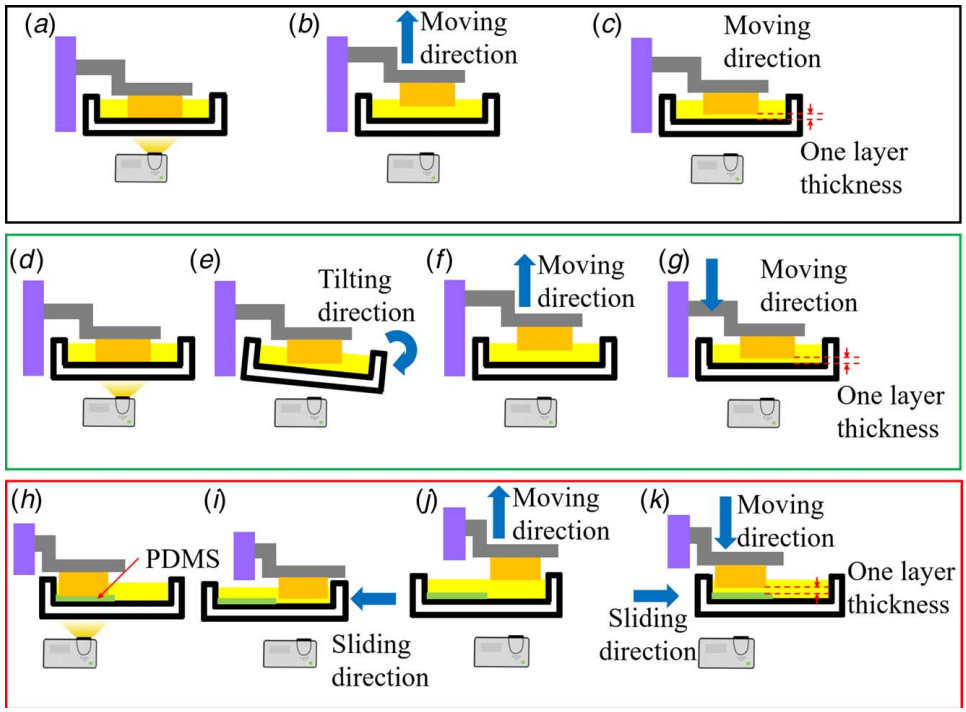

Fig. 2 Different mechanisms for the separation of cured layers from the constrained surface: (*a–c*) describe the pulling-up mechanism for the separation of cured layers. (*a*) Photocuring one layer by the projection of a mask image, (*b*) separating the cured layer from the resin vat by moving up the building platform, and (*c*) moving the building platform down to form a one-layer-thickness gap. (*d–g*) describe the tiling mechanism to achieve separation. (*d*) Photocuring one layer by the projecting of a mask image, (*e*) lowering the right side of the resin vat while pivoting the left side to achieve separation, (*f*) moving up the printing platform to facilitate the resin refill, and (*g*) moving down the printing platform to form a one-layer-thickness gap. (*h–k*) The two-channel system to achieve separation [14]. (*h*) Photocuring one layer by the projecting of a mask image, (*i*) sliding the resin vat in the horizontal direction to achieve the separation between the built layers and the vat using shear stress, (*j*) moving the building platform up, and (*k*) moving the building platform down to form a one-layer-thickness gap for the next layer.

building areas (e.g., 600 mm × 600 mm) used the free surface method. Since the required separation force in the constrained-surface method will exponentially increase for a large building area, how to deal with the separation force issue is one of the critical challenges to be addressed in developing future constrained-surface-based SL machines with a large building area.

Many attempts have been made to address this critical challenge before. Applying a suitable coating medium, e.g., a Teflon, silicon, or polydimethylsiloxane (PDMS) film, to the bottom surface of the resin vat is a widely used method to alleviate the pulling-up force [15,16]. Even with these coatings, the separation force is still considerably large for the direct pulling-up method. Therefore, some commercial systems (e.g., EnvisionTEC Ultra2 Printer) have adopted a slow pulling-up speed since a large pulling-up velocity will significantly increase the separation force [17]. The reduced moving-up speed will dramatically reduce the fabrication efficiency. Besides, the coated film has to be constantly stretched, and the cyclic loading to the film in the *Z* direction will make the film wrinkle after a certain time. Hence, the life of the separation film is usually limited.

Different motions of the resin vat or the building platform have also been proposed to reduce the separation force, such as tilting (Figs. 2(*d*)–2(*g*)) [17]. However, the tilting method performs poorly when the part cross-sectional area is large. Furthermore, the additional tilting motion increases the fabrication time, resulting in a reduction of productivity.

Applying the sliding motion based on a two-channel system has been presented by Zhou et al. [14], which showed using the

shearing force instead of directly pulling up can significantly reduce the separation force (Figs. 2(*h*)–2(*k*)). After the fabrication of one layer, the vat was slid in the horizontal direction, so the separation between the built layers and the vat can be achieved with shear stress. This two-channel system also incorporated an oxygen-aided inhibition mechanism discovered by Dendukuri et al. [18]. However, the PDMS is sandwiched between the liquid resin and vat. The isolated environment prevents the oxygen supply and the oxygen near the PDMS surface will be consumed. Pan et al. [8] presented a micro-hole-based approach to provide a sufficient and constant supply of oxygen to the PDMS medium. However, the required sliding motion should be at least the size of the building platform. Hence a longer fabrication time due to the sliding motion is required when the part cross-sectional area becomes larger.

Recently, Tumbleston et al. [19] proposed a continuous liquid interface production (CLIP) approach by using an oxygen-permeable Teflon AF 2400 film that creates a "dead zone" to inhibit photopolymerization. The thin inhibited layer allows the platform to move up continuously, which results in 25–100 times faster printing speed than other layer-based SL systems. Despite the improvement, the oxygen-permeable film will form a dome during the printing process because there is no constrained plane to define the formed layer. The gap between the film and the previously cured layers is not flat, which reduces the accuracy in the *Z* direction, especially for a part with a larger cross-sectional area.

To solve the dome effect of the oxygen-permeable film, Wang et al. developed an Active Separation Bottom-Up Stereolithography (ASBUS) process [20]. An empty area called the active zone is reserved between the Teflon film and the constrained plane. During the separation process, water is pumped into and out of the active zone to raise and then peel the film off the newly cured layer. The separation force is significantly reduced, and the dome effect is eliminated through this method. However, the additional pumping action complicates the structure and reduces manufacturing efficiency. Besides, this approach also faces the same disadvantage of the short-life film mentioned earlier for the film-based separation method.

Instead of using films or motions, another mechanism of using vibration to reduce the separation force was first proposed by Jin et al. [13]. The cyclic loading applied on the constrained surface will cause fatigue of the adhesive interface between the built part and the constrained surface. After enough cycles, the built layers can be separated entirely from the constrained surface. However, their vibration-assisted (VA) hardware design with the unrestricted reversed stress will cause unexpected damage to small features of the part. Also, the vibration effect on the large contact area and how the vibration parameters affect the separation performance were not studied. An improved design and a theoretical model to address the vibration effect are further developed in this paper.

2 Related Works

Our research in this paper focuses on the VA separation method and its underlying mechanism. A summary of the related work is presented in the section, including the application of vibration in other AM processes and the existing separation models used in other separation methods.

2.1 Vibration Used in Additive Manufacturing Processes. In addition to the aforementioned VA separation method in SL, vibration has been used in other additive manufacturing processes in the past decades to serve different roles. In many material jetting processes such as MultiJet Printing, the vibration of the piezoelectric unit of the printer head has shown the capability of precise control on the deposition of photocurable resin. Many investigations of vibration have been reported on facilitating the dry powder dispensing. For example, Yang and Evans [21] and Yang et al. [22] developed a powder-based additive manufacturing process, in which the vibration of an open capillary was used to switch powder flow on and off and to control the powder flowrate. The ultrasonic additive manufacturing (UAM) invented by Dawn White utilized ultrasonic vibration and pressure to build complex 3D components from metal foil. In the UAM process, ultrasonic vibration was locally applied to the materials to induce localized friction, enabling the breakage of oxide films, and then generated an atomic bond between layers [23]. In the binder jetting process, mechanical vibration has been reported to be an effective technique to compact the dispensed powder [24]. In the laser engineered net shaping (LENS) process, powder deposition defects such as uncertain pores, cavities, and residual stress always exist in the LENS fabricated parts. Cong and Ning [25] developed an ultrasonic vibration-assisted (UV-A) LENS process to reduce or eliminate these common defects. During the UV-A LENS process, the ultrasonic vibration of the building platform induced by a piezoelectric vibrator facilitates fluid material movements. The action improved the geometrical characteristics and mechanical properties of the metal parts.

2.2 Separation Models for Direct Pulling-up and Tilting Separation Methods. Besides the various methods developed to solve the separation issue in constrained-surface-based SL, researchers also examined the relationship between the separation force and the process parameters. They developed different models to characterize the separation process. A better understanding of the separation processes will significantly benefit the development of an intelligent control method that can be used in SL.

Huang and Jiang [16] developed a separation force monitoring system for the bottom-up constrained-surface SL with a silicone film as the coating material. Kovalenko et al. [26] experimentally verified the linear dependence between the pulling-up force and the built area on a bottom-up constrained-surface SL with a coated PDMS film. From the viewpoint of fracture mechanics, they used the crack initiation toughness to estimate the separation process. Based on the experimental results, they also found that the pulling-up force increased linearly with the contact area. Besides, their study indicated that the projected images with different shapes of the same area resulted in the same separation force. The geometry only affected the shape of the force-platform displacement profile.

Based on the measured force data, Zhou et al. [14] reported that the separation force was affected by several factors, including exposure time, image area, and image geometry. The exposure time effect was explained from the perspective of energy. The image geometry, unlike the conclusion drawn by Huang and Jiang, was found to have impact on the peak force but not as clear as the factors of the exposure time and image area.

Liravi et al. [27] characterized the separation of the cured layer from the PDMS coated resin vat as the delamination of a laminated composite structure based on fracture mechanics. The method for failure analysis of the laminated composite structure was developed to analyze the pulling-up separation in the bottom-up based SL. The cohesive zone model (CZM) was adopted to predict the separation behavior of different pulling-up velocities. The constitutive parameters for the CZM were estimated from the experimentally measured pulling-up force. The finite element simulation showed that the CZM was eligible for simulating the separation force under different pulling-up velocities. It should be noted that the cohesive zone does not represent any physical material. This zone can be perceived as a zone of vanishing thickness at the interface between the two separate parts. Hence, CZM can be applied to different materials (e.g., the photocurable polymer and the coating media) by changing the material parameters or the cohesive law that defines the behavior of the cohesive zone.

From the fluid mechanics perspective, Pan et al. [8] used Navier–Stokes equations to study how pulling-up velocity affects the pulling-up force under the circumstance that the oxygen-aided inhibition effect is present. The result indicated the same conclusion that an increasing pulling-up speed will lead to a larger separation force.

Wu et al. [28] built a constrained-surface SL based on the tilting separation mechanism and applied the CZM in the analysis of the separation force. Experimental studies on the effects of different building areas, part orientations, coating films, and tilting velocity on the separation force were conducted by experimentally collecting the force data. The study results can be used in choosing reasonable process parameters for the constrained-surface based SL process.

2.3 Contributions. The above researches will help improve the reliability and throughput of the constrained-surface-based SL process. However, no analytical model that describes the VA separation mechanism was found. Consequently, it is challenging to choose parameters for a given building area due to the lack of separation force model. Our work presented in the paper aims to address this critical issue.

The main objective of this work is to present a new VA separation hardware design for the bottom-up-based SL process and to identify an analytical model based on the mechanics of fatigue fracture. Accordingly, the influence of various factors, including layer area, layer shape, and cyclic loading parameters on the VA separation process, will be evaluated. The obtained knowledge from the study will help the development of the VA separation method for the constrained-surface-based SL process.

The rest of the paper is organized as follows. In Sec. 3, different fatigue models are compared, and the stress-based model is selected to characterize the VA separation. After the theoretical study, a prototype design that incorporates the piezo-driven vibration is presented for the vibration-assisted SL (VA-SL) process. In Sec. 4, comprehensive separation experiments with the vibration of different cyclic loading frequency and amplitude are conducted by collecting the force data sequence in fabricating a designed part. The performed experiments on different exposure areas, image shape, and shape topology are also presented in this section. In Sec. 5, the knowledge-based rules are summarized to answer how to set process parameters for the VA separation-based SL process. A correspondingly developed algorithm is presented with a test case to demonstrate the effectiveness of the algorithm. The comparison between the pulling-up separation with and without the VA method is also presented in the section. Finally, conclusion and future work are given in Sec. 6.

3 Vibration-Assisted Separation in the Constrained-Surface-Based SL Process

3.1 Analytical Model of the Vibration-Assisted Separation Method. In the presented work, we incorporated the vibration fatigue mechanism in the pulling-up separation process so that the separation force can be significantly reduced. According to Liravi et al. [15,27] and Ye et al. [17], the direct pulling-up separation in the constrained-surface-based SL has been successfully demonstrated to be a fracture behavior between different materials. After the fabrication of each layer, the newly cured layer and the coated film will form a laminated composite structure. Therefore, the failure analysis of the laminated composite structure can be analyzed using a method such as CZM. Similar to the brittle fracture that happened at the interface between the cured part and the coating media during the direct pulling-up or the tilting methods, vibration can also be used to break the interface. The main difference is that the pulling-up and tilting process is the one-shot separation, while the VA separation results from progressively accumulated physical damage under the cyclic loading.

From this perspective, the VA separation will be modeled using the concept of the vibration fatigue failure process. There exist three major approaches that have been widely used to analyze fatigue-related failures [29–34].

(1) The stress-based approach directly relates the fatigue life with the nominal (average) stress and the stress amplitude in the affected region of the engineering component. The stress-fatigue life (S-N) curve is the basis for the stress-based analysis. The effects of variables such as stress level and geometry will be reflected in the trends or intercepts of the S-N curves. Generally, this approach is mainly used to predict fatigue life. It is also applicable to complex geometry. Since we care more about the separation force and separation time when evaluating a separation method and the force data can be easily measured during the separation process, the stress-based approach is a suitable candidate for our purpose.
(2) The strain-based approach is similar to the stress-based approach, but it explores strain versus fatigue life. Instead of the nominal stress versus fatigue life curve, the strain versus fatigue life curve is used as the basis in the analysis model. Based on the analysis of local yielding, the strain-based method gives improved estimates for ductile materials under short fatigue cycles. However, the method is not suitable for the detachment of the adhesive bonding between the solidified resin and the coated film because little yielding phenomenon occurred.
(3) The crack-growth-based approach mainly focuses on the evolution of the crack growth rate. Based on the stress intensity factor, the severity of initially existing defects, such as cracks sustained during service, can be estimated. The estimation is important in setting periodic safety inspection interval or damage-tolerant design, which requires structures to be able to survive even in the presence of growing cracks. However, this method cannot predict crack initiation and can only predict the propagation of the existing crack. Therefore, pre-existing crack and definite propagation direction are required in this method [17]. However, no initial crack exists before separation in the VA separation-based SL. The crack initiation position and propagation direction are stochastic in the separation process. Also, it is challenging to integrate the equipment that can measure the crack growth rate into a SL machine.

In summary, a stress-based fatigue model will be applied to our VA separation system and the related experiment design. Since the stress-based fatigue model was derived from the S-N curve, two force sensors were mounted in our prototype system to measure and control the force applied on the part-film separation portion throughout the whole fatigue life in real time. In the stress-based fatigue theory, cyclic stress amplitude ΔS shown in Fig. 3(*c*) has a strong relationship with fatigue life. The fatigue life was counted by the number of load cycles. High load frequency can shorten the required time to accomplish the break of the component. Therefore, compact equipment that can provide high-frequency load is desired in the VA-SL system. For this reason, two piezoelectric actuators were incorporated in the prototype system to provide cyclic load at high frequency. Besides, the pre-stress S_{min} applied to the component (see Fig. 3(*c*)) also played a vital role in determining fatigue life. The pre-stress was achieved by stretching the part-film interface when adding the vibration. Secs. 3.2 and 3.3 will give a detailed description of the whole prototype system design and the related process investigation using the developed prototype system.

3.2 Design of Stereolithography System With Vibration-Assisted Separation Mechanism. There are many possible configurations to achieve the VA separation mechanism design. One configuration for the VA-SL system is shown in Fig. 3. Other variations of the VA configuration can be made based on the presented design logic.

The cyclic load was provided by two piezoelectric actuators (MTKK16S400F170R, Mechano Transformer Corp., Tokyo, Japan). The transparent glass resin vat coated with Teflon film (Shanghai Witlan Industry Corp., Shanghai, China) was connected with the two piezoelectric actuators directly, and then mounted to a fixed aluminum frame. The piezoelectric actuators were powered by the PiezoMaster power amplifier (VP7206-24K150, Viking Industrial Products, Marlboro, MA). The piezoelectric actuators

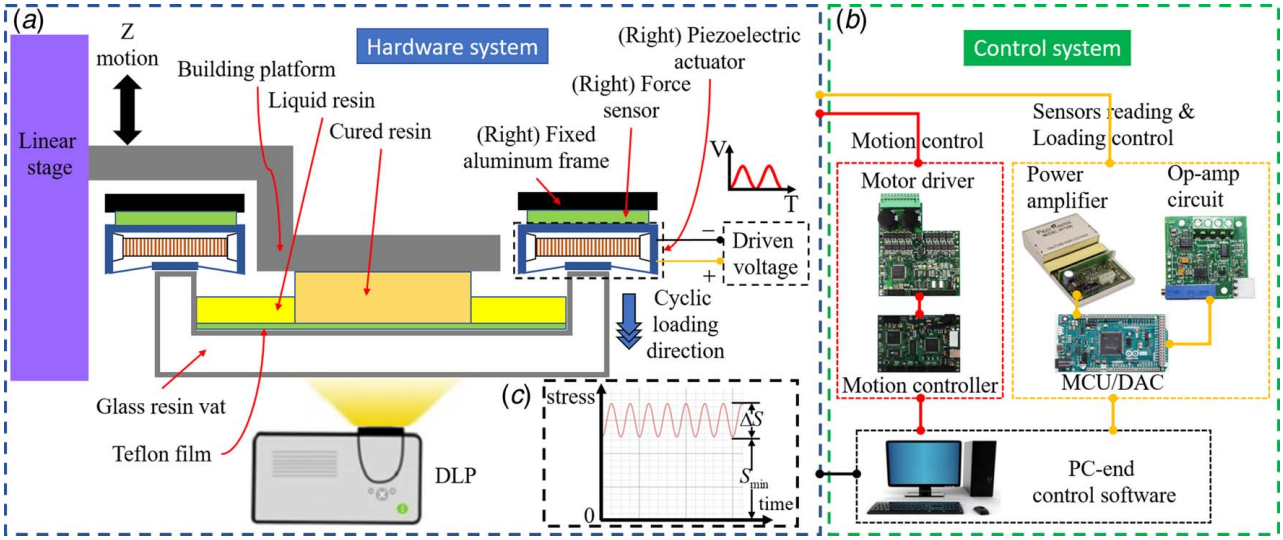

Fig. 3 The prototype system using the VA separation mechanism: (*a*) the hardware of the VA separation-based SL with two piezoelectric actuators, (*b*) the control and circuits required in the VA separation-based SL system, and (c) an illustration of cyclic loading. Cyclic stress amplitude ΔS represents the interval between the maximum and minimal stresses and S_{min} represents the minimal stress.

only provided load downward once energized, keeping its top frame static. The cyclic loading was controlled by the digital-to-analog converter (DAC) output of an Arduino microcontroller. By varying the driving voltage, the piezoelectric actuator provided different forces onto the newly cured layers. Two force sensors (FlexiForce A201 Sensor, Tekscan, Inc., South Boston, MA) were sandwiched between the fixed aluminum frame, and the piezoelectric actuators were used to measure the separation force in real time. Based on the feedback of the force sensors, we controlled the force applied to the part-film interface. An Op-amp circuit (FlexiForce Quickstart Board, Tekscan, Inc., South Boston, MA) amplified and converted the sensor signal to voltage. The Arduino microcontroller collected the voltage data through its analog-to-digital converter (ADC) inputs and then sent the readout to a computer. Since the resin vat was only fixed at the top, the pulling force from the part was transferred to the sensors when the building platform raised. Thus, the sum of the two measured forces is equal to the separation force between the newly cured layers and the constrained vat surface. The resultant force data sequence reflected the separation process and formed the basis of our analysis. The linear stage to mount the building platform was driven by a KFLOP motion controller and a SnapAmp amplifier (Dynomotion Inc., Calabasas, CA). The 405 nm ultraviolet (UV) DLP projector served as the irradiation light source. A self-developed software system synchronized the whole experimental process, including sending commands to the microcontrollers and the DLP projector and acquiring data from the sensors.

3.3 3D Printing Process With the Vibration-Assisted Separation Method. The VA separation mechanism works with the typical bottom-up SL process. A detailed description of the VA-SL process is given as follows:

(1) When the fabrication of one layer begins, the DLP projector projects a mask image to photocure a thin layer of liquid resin. After a certain exposure time, the liquid resin is solidified between the previously cured layers and the coated film (using Teflon), as shown in Fig. 4(*a*).
(2) After the curing process, a computer begins to read and record the readouts of the two force sensors until the end of the separation process (see Figs. 4(*b*)–4(*e*)). Meanwhile, the building platform moves up a small distance Δx_1 mm to provide a pre-stress S_{min} to the separation region. Once the specified pre-stress S_{min} has been achieved, the building platform will be held in the position, as seen in Fig. 4(*b*).
(3) When the movement of the building platform is complete, the controller drives the piezoelectric actuator with cyclic voltage $V = -V_a \cos \omega t + V_a$. The interface between the newly cured layers and the coated film will be under cyclic load. The peak voltage V_a is determined by the feedback of the force readout. The state will last for a time Δt so that the fatigue failure occurs within this period. After the period of Δt, the piezoelectric actuator is disabled. This process can be seen in Figs. 4(*c*) and 4(*d*). The force data have been continuously recorded during this period.
(4) After the piezoelectric actuator is disabled. The platform moves up a sufficient distance Δx_2 to make sure the part-film interface is separated if the fatigue life is longer than Δt and facilitates the resin refilling, as shown in Fig. 4(*e*). At the end of the step, the process of collecting the force data will be stopped. Till now, the whole separation process is complete.
(5) Finally, move down the building platform by Δx_2 to form a one-layer-thickness (Δl) gap, as shown in Fig. 4(*f*). Now the setup is ready for the curing of the next layer (Fig. 4(*a*)).

4 Experimental and Analysis Results

4.1 Experimental Design. For the VA separation method, many factors may affect the required separation time, including loadings condition (frequency, cyclic stress amplitude, and pre-stress), exposure area sizes, geometric topologies, and geometric shapes. In order to study the relationship between the separation time and these factors, five test cases were designed. They are discussed as follows:

- Test case 1—different loading frequency

  To study the frequency effect, a cylinder was designed and fabricated using the VA separation-based method with different loading frequencies. The driving voltage of the piezoelectric actuator was fixed, while the frequency was varied. The parameter settings are listed in Table 1. There were eight parameter settings in total, and each experiment was repeated ten times. The first 20 layers were printed as a base. Data collected from the rest layers were used in the analysis. The parameter sets were used alternately during the fabrication to

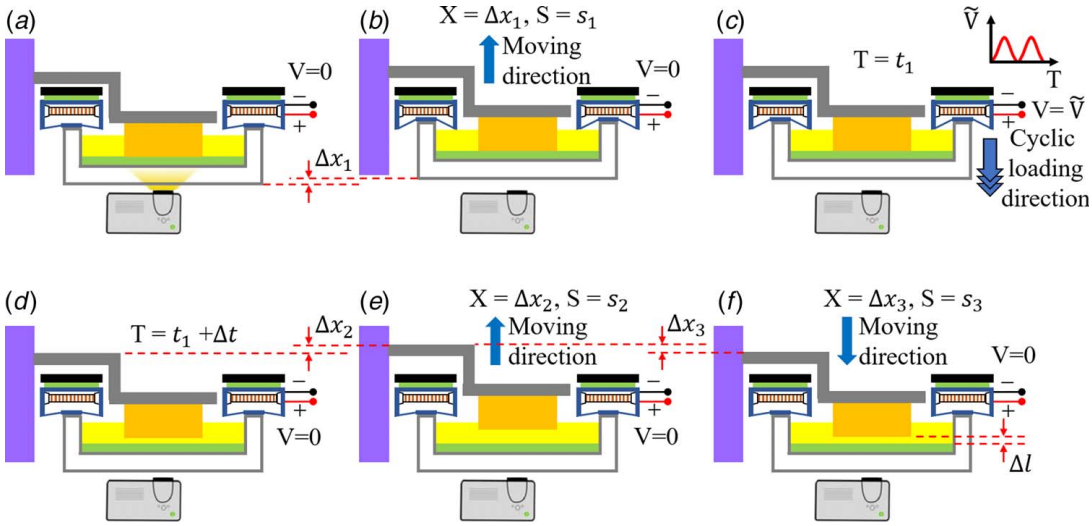

Fig. 4 3D printing process with the VA separation-based method: (*a*) projecting a mask image to cure the liquid resin, (*b*) moving up the building platform by a small distance Δx_1 mm to provide a pre-stress S_{min} to the separation region, (*c*) applying cyclic load by driving the piezoelectric actuator with cyclic voltage V, (*d*) after the period of Δt, the part-film interface is separated, (*e*) moving up the building platform by Δx_2 mm to facilitate resin refill, and (*f*) moving down the building platform by Δx_2 mm to form a one-layer-thickness gap (Δl)

Table 1 Parameter setting for test case 1

Exposure area A (mm^2)	2189
Height (mm)	5
Layer thickness Δl (mm)	0.05
Voltage (V)	150
Pre-stress S_{min} (Pa)	0
Frequency (Hz)	100, 200, 300, 400, 500, 600, 700, 800

avoid the errors induced by the height. The detailed result and analyses are presented in Sec. 4.2.1.

- Test case 2—different cyclic load amplitude and pre-stress

  To compare the effect of the cyclic stress amplitude ΔS and the pre-stress S_{min} on the separation time, a cylinder was fabricated using the VA separation-based method with different process parameters. The frequency was fixed at 500 Hz, and the loading force was varied by controlling the driving voltage of the piezoelectric actuator. The parameter settings are listed in Table 2. The detailed result and analysis are presented in Sec. 4.2.2.
- Test case 3—different exposure area

  Following the same process described in test case 1, cylinders of various diameters were printed to investigate the effect of exposure areas on the separation performance, including the separation force and time. Under the same voltage, the stress will decrease with the increase of exposure areas. Thus, the pre-stress was raised to shorten the fatigue life. The parameter settings are shown in Table 3. The corresponding results are described in Sec. 4.2.3.

Table 2 Parameter setting for test case 2

Exposure area A (mm^2)	2189
Height (mm)	5.5
Layer thickness Δl (mm)	0.05
Cyclic stress amplitude ΔS (Pa)	2976, 5952, 8928
Pre-stress S_{min} (Pa)	0, 1600, 3200
Loading frequency (Hz)	500

Table 3 Parameter setting for test case 3

Exposure area A (mm^2)	2189	4378	6567
Height (mm)	5.5	5.5	5.5
Layer thickness Δl (mm)	0.05	0.05	0.05
Cyclic stress amplitude ΔS (Pa)	2976, 5952, 8928	1488, 2976, 4464	992, 1984, 2976
Pre-stress S_{min} (Pa)	0, 1600, 3200	4800, 6400, 8000	9600, 11,200, 12,800
Loading frequency (Hz)	500	500	500

- Test case 4—different geometric topologies of the same area size

  The effect of geometric topologies on the VA separation behavior was studied by fabricating a larger single cylinder and smaller cylinder arrays following the aforementioned process. Each cylinder array is composed of a set of smaller cylinders of the same area. The sum of the cross-sectional area of each cylinder array is equal to the area of the larger single cylinder. The parameter settings are shown in Table 4, and the test results are discussed in Sec. 4.2.4.
- Test case 5—different geometric shapes of the same area size

  The geometric shape may also affect the VA separation time. Thus, various shapes of the same area were designed to explore the influence of the geometric shapes, including circle, ring, triangle, square, pentagon, and pentagram. The corresponding parameter settings are listed in Table 5. The test results are discussed in Sec. 4.2.5.

Table 4 Parameter setting for test case 4

Exposure area A (mm^2)	4378	4378	4378
Number of cylinders	1	2	4
Height (mm)	3	3	3
Layer thickness Δl (mm)	0.1	0.1	0.1
Cyclic stress amplitude ΔS (Pa)	4464	4464	4464
Pre-stress S_{min} (Pa)	8000	8000	8000
Loading frequency (Hz)	500	500	500

Table 5 Parameter setting for test case 5

Shape	Circle	Ring	Triangle	Square	Pentagon	Pentagram
Exposure area A (mm^2)	2189	2189	2189	2189	2189	2189
Height (mm)	3	3	3	3	3	3
Layer thickness Δl (mm)	0.1	0.1	0.1	0.1	0.1	0.1
Cyclic stress amplitude ΔS (Pa)	5952	5952	5952	5952	5952	5952
Pre-stress S_{min} (Pa)	0	0	0	0	0	0
Frequency (Hz)	500	500	500	500	500	500

4.2 Result Analysis

4.2.1 Different Loading Frequency. To identify the optimal loading frequency, we printed the same part with a gradually ramped-up frequency from 100 Hz to 800 Hz under the same driving voltage 150 V. The corresponding force amplitude and separation time data of different frequencies are plotted in Fig. 5.

From Fig. 5, we can see the loading frequency and force amplitude are coupled in the current VA-SL system. The increase in the loading frequency from 100 Hz to 500 Hz leads to a reduction in separation time. However, when the frequency is higher than 500 Hz, the separation time starts to increase. The time increase is because the increase in frequency results in a dramatic decrease in amplitude if the frequency is higher than 500 Hz. Therefore, after synthetically considering the effect of frequency on the amplitude range and separation time, we decided to use 500 Hz as the loading frequency to fabricate all the rest test cases.

4.2.2 Different Cyclic Stress Amplitude and Pre-Stress. The test results regarding loading amplitude and pre-stress effect on the number of cycles required in the VA separation method are listed in Table 6 with a diagram shown in Fig. 6.

As shown in Fig. 6(*a*), the peak stress level S_{max} of the same pre-stress S_{min} and the number of cycles N_f approximate a straight line on a log-log plot. Therefore, Eq. (1) can be used to fit the obtained data. The bar chart Fig. 6(*b*) reflects the number of cycles under different cyclic stress amplitude ΔS. For the same pre-stress, larger

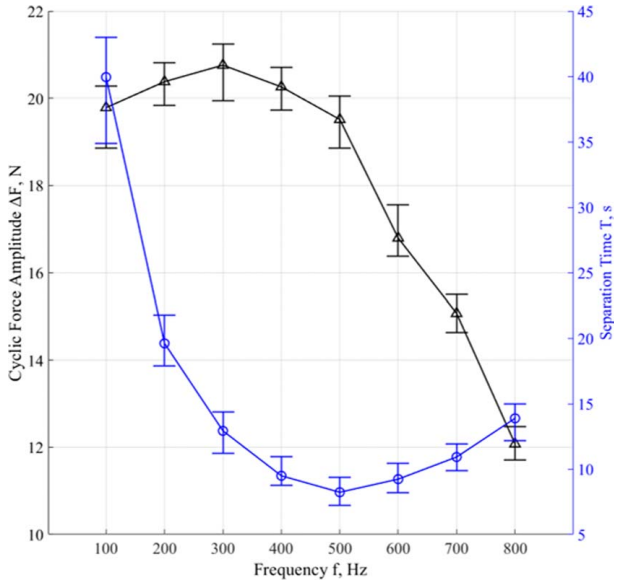

Fig. 5 Relationships between force amplitude and separation time related to frequency in the current setup

Table 6 Test results of the number of loading cycles to separation under different loading conditions

Number of cycles N_f		Cyclic stress amplitude ΔS (Pa) 2976	5952	8928
Pre-stress S_{min} (Pa)	0	$45{,}226.4^{+5706.6}_{-6520.4}$	$9611.4^{+1168.6}_{-1496.4}$	$4110.5^{+576.5}_{-489.5}$
	1600	$31{,}173.2^{+6069.8}_{-4348.2}$	8000^{+880}_{-765}	$3767.6^{+566.4}_{-541.6}$
	3200	$21{,}830.2^{+3139.8}_{-2916.2}$	$7103.4^{+925.6}_{-624.4}$	$3208.9^{+271.1}_{-492.9}$

cyclic stress amplitude can reduce the number of cycles required to achieve total separation and therefore shorten the separation time (Fig. 6(*b*)); however, it also leads to larger peak stress and separation force (Fig. 6(*a*)). For the same cyclic stress, larger pre-stress can also reduce the separation time (Fig. 6(*b*)). However, the peak stress level will also be larger.

$$S_{max} = AN_f^B \tag{1}$$

Both factors have a similar effect. However, for the same maximum stress, which is the sum of the cyclic stress and the pre-stress, larger cyclic stress and lower pre-stress will reduce the number of cycles. The reduction qualitatively indicates that the contribution of the cyclic stress on the separation is more significant than the pre-stress, and the cyclic stress factor is more significant than the pre-stress to the separation time.

Therefore, the Walker equation [33] was utilized to consider the effect of the pre-stress quantitatively

$$\overline{\Delta S} = (S_{min} + \Delta S)^{1-\gamma}\Delta S^{\gamma} = S_{max}^{1-\gamma}\Delta S^{\gamma} \tag{2}$$

where $\overline{\Delta S}$ is the equivalent cyclic stress range as if the pre-stress equals 0, the value of constant γ is limited to the range [0,1]. γ can be viewed as a measurement of the sensitivity to the pre-stress. Low values γ correspond to high sensitivity, and values approaching 1 to low sensitivity. If $\gamma = 0$, then it indicates the pre-stress, and the cyclic stress takes equivalent effect. $\gamma = 1$ represents the pre-stress has no effect. Therefore, γ value allows a quantitative estimation of the two factors. Combine Eqs. (1) and (2), and then solve for N_f:

$$N_f = \left[S_{max}^{1-\gamma}\Delta S^{\gamma}\frac{1}{A}\right]^{1/B} \tag{3}$$

Taking the logarithm to the base 10 of both sides will give

$$\log(N_f) = \frac{1-\gamma}{B}\log(S_{max}) + \frac{\gamma}{B}\log(\Delta S) - \frac{1}{B}\log(A) \tag{4}$$

By doing multiple linear regressions with variables $\log(S_{max})$, $\log(\Delta S)$, and $\log(N_f)$, we have

$$\gamma = 0.5637 \tag{5}$$

Therefore, the equivalent cyclic stress amplitude can be obtained. The converted points from different pre-stress form a straight line (Fig. 7). With the constant γ, for the given circle mask image, the separation time under different cyclic loading conditions can be estimated using Eq. (6)

$$\log(N_f) = \log(ft) = -0.93\log(S_{max}) - 1.20\log(\Delta S) + 12.06 \tag{6}$$

4.2.3 Different Area Sizes. The test results regarding the effect of the exposure area on the number of cycles required in the VA separation method are listed in Table 7 and diagrammed in Fig. 8.

As shown in Fig. 8(*a*), similar behavior as the ones in Fig. 6(*a*) can be observed, except a higher pre-stress has to be applied for a larger area to complete the separation within a reasonable time. The peak stress level S_{max} of the same pre-stress S_{min} and the cycles to separation N_f approximate a straight line for different

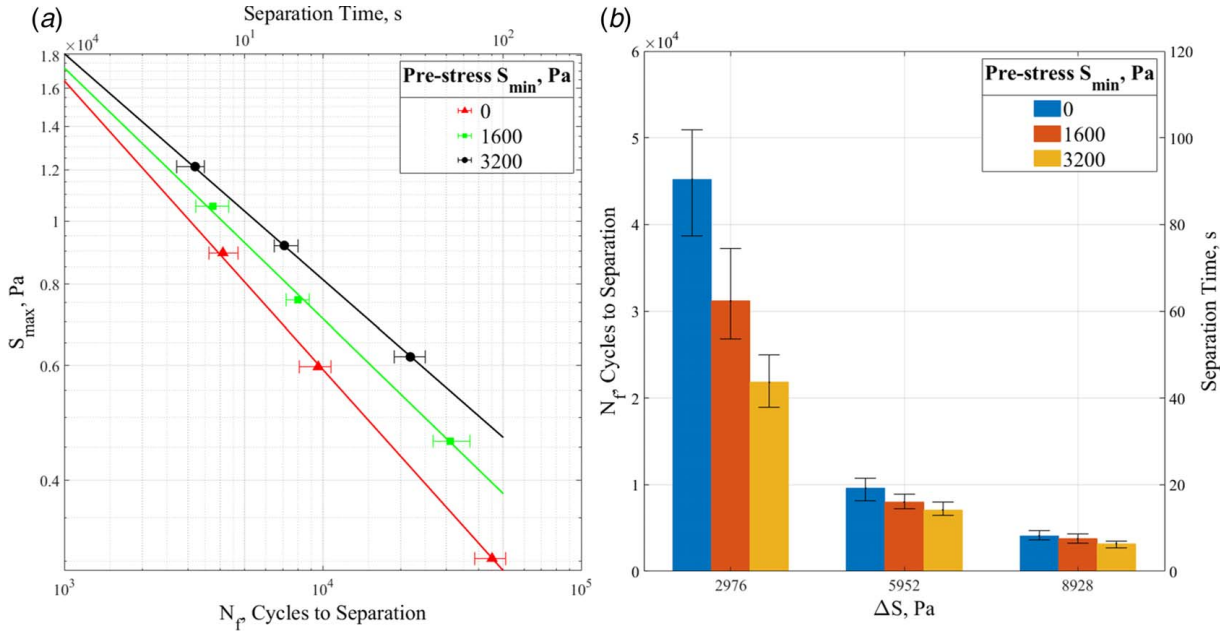

Fig. 6 (*a*) S–N curves and the corresponding separation time under different pre-stresses and (*b*) cyclic numbers and the corresponding separation time under different pre-stress

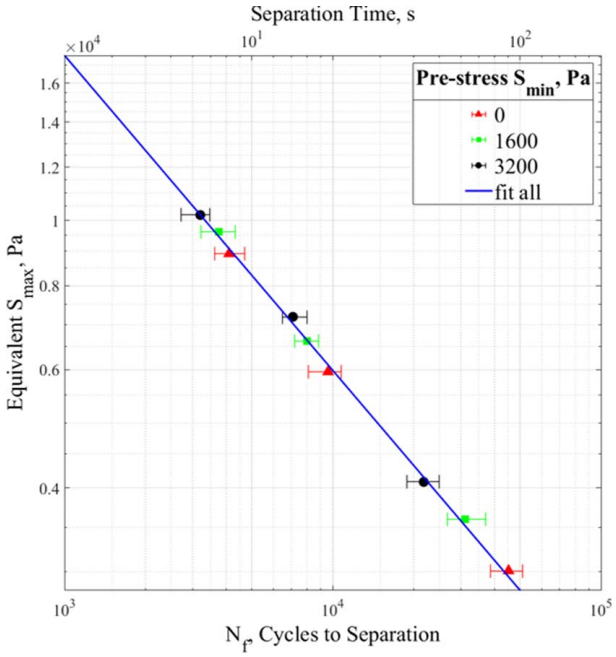

Fig. 7 Equivalent S–N curve and corresponding separation time under different pre-stresses

area sizes on a log-log plot. By applying the Walker equation and multiple linear regression, we can get a straight line fitted by the points of zero stress amplitude and the equivalent zero stress amplitude, as shown in Fig. 8(*b*). γ equals 0.5622, which approaches the previous value calculated in Sec. 4.2.2. R^2 is 0.94, indicating a strong linear relationship of the testing results. Therefore, for the individual circle pattern of different areas under different loading conditions, the separation time can be estimated by the following linear regression model:

$$\log(N_f) = \log(ft) = -0.81\log(S_{max}) - 1.04\log(\Delta S) + 11.01 \quad (7)$$

Table 7 Test results of the number of loading cycles to separation for different area sizes

		Cyclic stress amplitude ΔS (Pa)		
Cyclic number N_f		2976	5952	8928
Exposure area A (mm^2): 2189				
Pre-stress S_{min} (Pa)	0	$45{,}226.4^{+5706.6}_{-6520.4}$	$9611.4^{+1168.6}_{-1496.4}$	$4110.5^{+576.5}_{-489.5}$
	1600	$31{,}173.2^{+6069.8}_{-4348.2}$	8000^{+880}_{-765}	$3767.6^{+566.4}_{-541.6}$
	3200	$21{,}830.2^{+3139.8}_{-2916.2}$	$7103.4^{+925.6}_{-624.4}$	$3208.9^{+271.1}_{-492.9}$
		Cyclic stress amplitude ΔS (Pa)		
Cyclic number N_f		1488	2976	4464
Exposure area A (mm^2): 4378				
Pre-stress S_{min} (Pa)	4800	$36{,}754.1^{+4903.9}_{-4460.1}$	$19{,}087.4^{+1910.6}_{-2001.4}$	$10{,}551.4^{+1045.6}_{-836.4}$
	6400	$31{,}499.1^{+4658.9}_{-4323.1}$	$16{,}927.4^{+1570.6}_{-1849.4}$	$9612.5^{+934.6}_{-996.4}$
	8000	$27{,}354.1^{+4303.9}_{-3178.1}$	$15{,}067.4^{+1430.6}_{-1481.4}$	$8561.4^{+784.6}_{-746.4}$
		Cyclic stress amplitude ΔS (Pa)		
Cyclic number N_f		992	1984	2976
Exposure area A (mm^2): 6567				
Pre-stress S_{min} (Pa)	9600	$35{,}142.9^{+4374.1}_{-4242.9}$	$21{,}454.3^{+2244.7}_{-2167.3}$	$14{,}866.2^{+1225.8}_{-1578.2}$
	11,200	$32{,}362.9^{+2988.1}_{-4142.9}$	$20{,}118.1^{+2080.9}_{-2331.1}$	$13{,}186.2^{+1005.8}_{-1598.2}$
	12,800	$28{,}242.9^{+3274.1}_{-3022.9}$	$18{,}448.1^{+1750.9}_{-1661.1}$	$10{,}786.2^{+1205.8}_{-898.2}$

4.2.4 Different Geometric Topologies. For a given cross-sectional area, the test result for different geometric topologies is presented in Table 8 and Fig. 9.

From Fig. 9, the average separation time decreases as the number of cylinders increases, which can be explained by the increase in the number of individual circles. The total fatigue life can be divided into two stages—the crack formation and crack propagation [34]. According to Liravi et al. [15], cracks initiate from the boundary

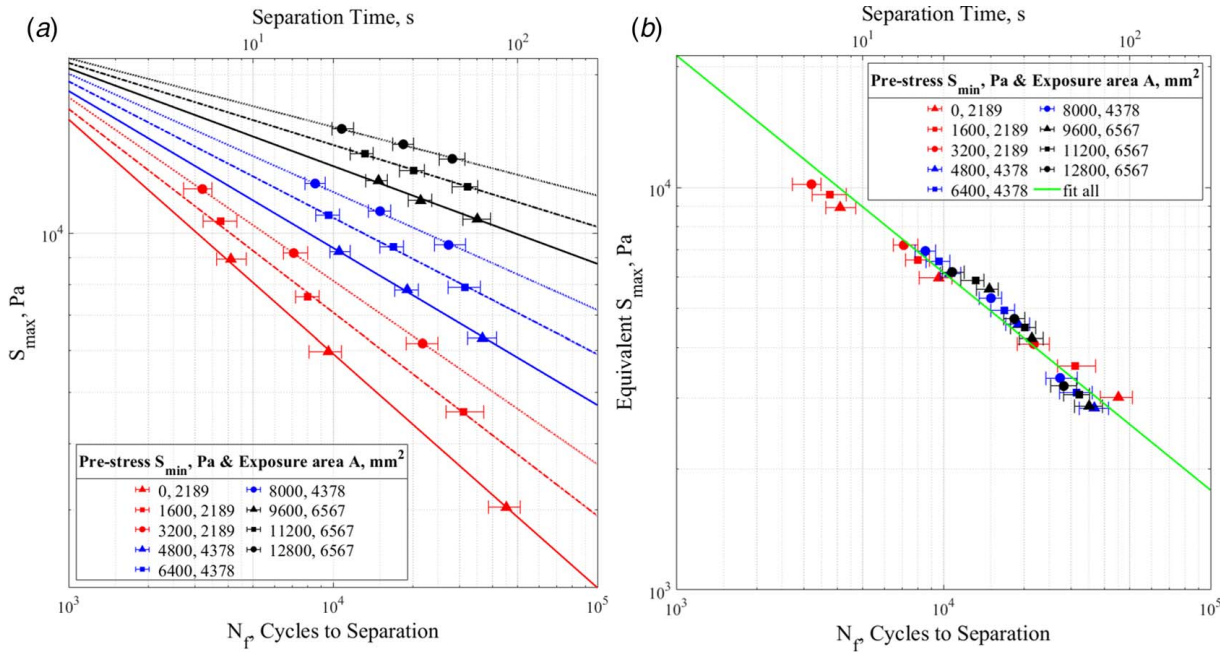

Fig. 8 (*a*) S–N curves and the corresponding separation time for different pre-stresses and exposure areas and (*b*) equivalent S–N curve and the corresponding separation time for different pre-stresses and exposure areas

Table 8 Test results of the number of loading cycles to separation for different geometric topologies

Cylinder number	1	2	4
Cyclic number N_f	$8561.4^{+784.6}_{-746.4}$	$7795.1^{+646.9}_{-769.1}$	$7207.1^{+530.9}_{-567.1}$

of the specimen because of the local stress concentration (see Fig. 10). For the same shape and area, the pattern with more separate parts forms a crack tip earlier under the same loading condition, which explains why the crack tip arises first in the four-cylinder array followed by the two-cylinder array and the last is the single-cylinder as indicated in Fig. 10. Besides, more than one crack initiation was observed for the two- and four-cylinder arrays in Fig. 10.

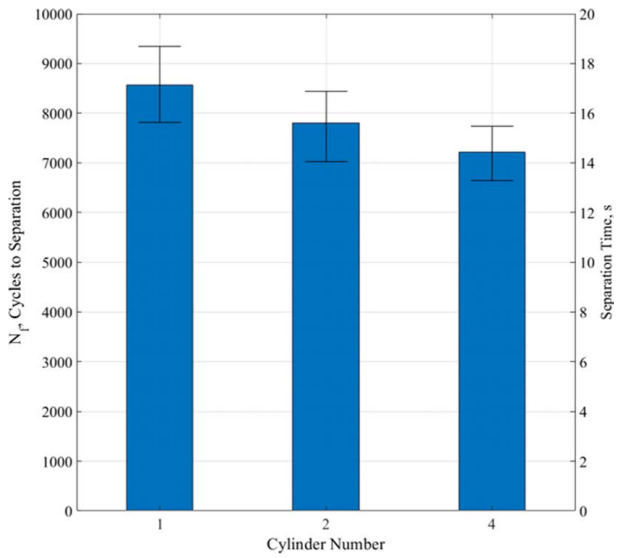

Fig. 9 Cyclic number (left) and the corresponding separation time (right) for different geometric topologies including single cylinder, two-cylinder array, and four-cylinder array, respectively

More crack initiations also sped up the propagation process and shortened the separation time.

4.2.5 Different Shapes. The test result for different geometry is presented in Table 9 and Fig. 11.

The separation time varied for different shapes when using the VA separation-based method. Among the different shapes, the circle took the longest time for separation. The test results indicated that a longer separation time was required for the shapes with smooth borders to separate, compared with the shapes with sharp corners or holes, which is compatible with the findings reported in Liravi et al. [15] and Lin and Yang [35].

For the same boundary shape, the difference between circle and ring mainly stems from the crack propagation stage [36]. The most important difference of the circle and ring in terms of crack propagation is that, for the circular shape, the crack propagates toward the middle section; in comparison, for the ring shape, the crack propagates from the two free openings and propagates toward the inner portion individually (Fig. 12). Hence, the different boundary conditions lead to different crack growth rates.

Shapes with sharp corners form crack tip more easily. The difference is especially obvious in the case of pentagram and triangle (Fig. 12). Therefore, the time for crack initiation was shorter for pentagram and triangle than the other four shapes. Besides, multi-site crack initiation was also observed in the pentagram, which reduced the time for crack propagation through the layer. Since the total separation time is equal to the life of the crack formation and propagation, the pentagram and triangle took the shortest time for the layer separation.

5 Process Settings for VA-SL and Comparison Study

5.1 Comparison of the Separation Forces in the Direct Pulling-Up and Vibration-Assisted Separation Methods. To compare the separation forces in the direct pulling-up and VA separation-based methods, three cylinders with different diameters were fabricated using the two separation methods. The separation force data are listed in Table 10 and plotted in Fig. 13.

To make the results from the two different separation methods comparable, the pulling-up velocity is set to a slow speed so that

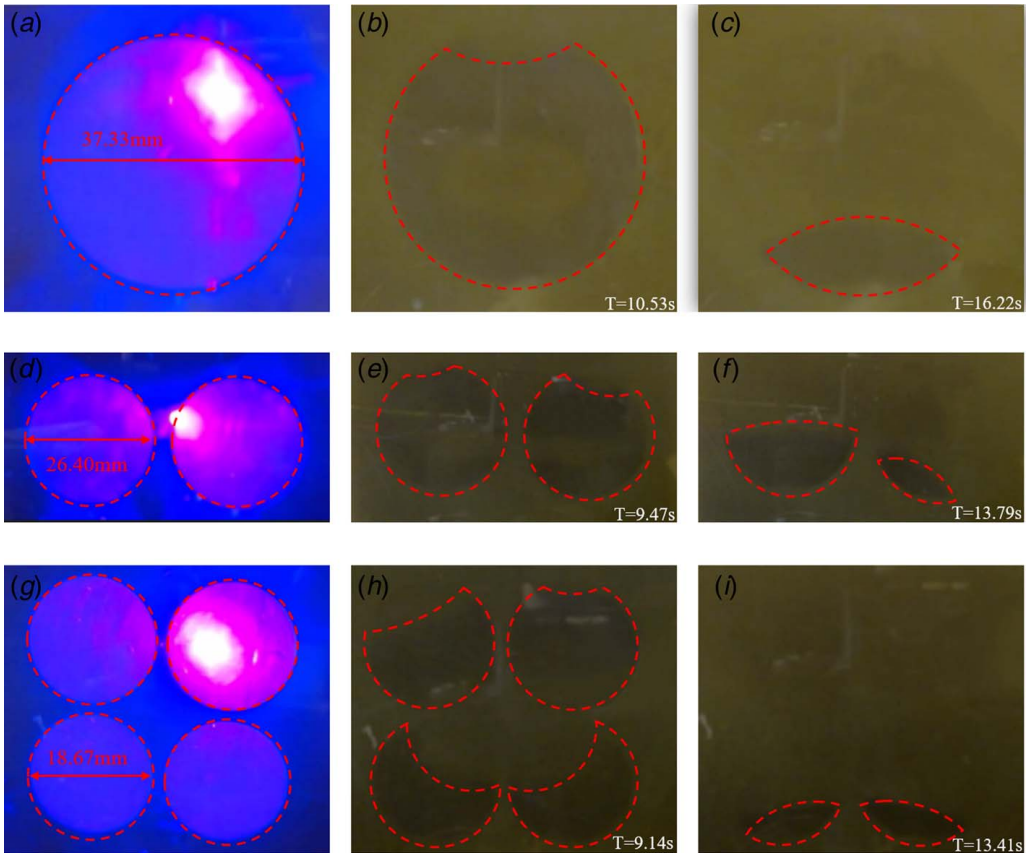

Fig. 10 Crack initiation and propagation of patterns with different geometric topologies, including (*a–c*) single cylinder, (*d–f*) two-cylinder array, and (*g–i*) four-cylinder array, respectively

Table 9 Test results of the number of loading cycles to separation for different shapes

Shape	Circle	Ring	Triangle
Cyclic number N_f	$9611.4^{+1168.6}_{-1496.4}$	$8874.8^{+816.2}_{-1325.8}$	$4726.4^{+326.6}_{-677.4}$
Shape	Square	Pentagon	Pentagram
Cyclic number N_f	7335^{+802}_{-990}	6684^{+768}_{-571}	$4066.4^{+343.6}_{-393.4}$

their separation time is approximately the same. As shown in Fig. 13, with the VA separation-based method, the separation force is reduced by around 75% for different layer areas, which demonstrates the effectiveness of the VA separation method. The smaller separation force will make the constrain-surface-based SL process more reliable.

5.2 Algorithm on the Process Setting for VA-SL. To integrate the VA separation mechanism into a slicer for the SL process, an algorithm on the process settings for the VA-SL process was developed (Fig. 14), which aims to provide different separation time options for users. For a model with a large layer area or features that can be easily broken during fabrication, a longer separation time needs to be selected so the separation force will be sufficiently small to increase the reliability of the fabrication process. In comparison, for a model with a relatively small area, a short separation time can be applied to increase fabrication efficiency.

In Fig. 14, the total cross-sectional area can be calculated from the mask image of each layer. If the cross-sectional area is smaller than the pre-defined area limit, the direct pulling-up

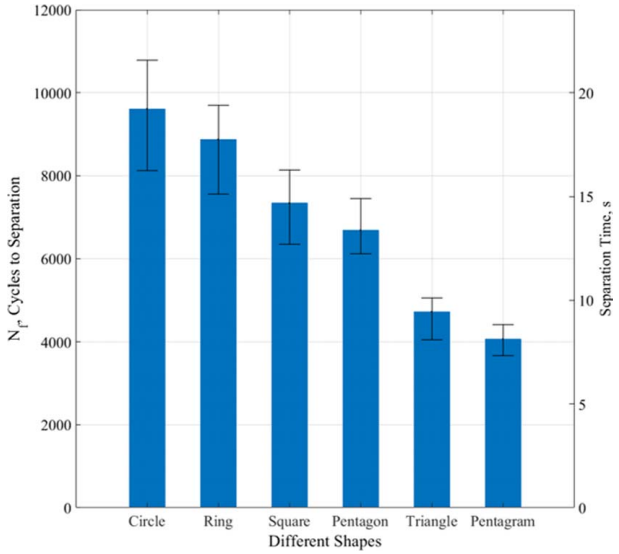

Fig. 11 Cyclic number (left) and the corresponding separation time (right) for different shapes

without vibration will be applied; otherwise, the VA separation method will be used. The total cross-sectional area was converted to a circle with an equivalent area. Then the cyclic stress amplitude was estimated based on the given separation time requirement and the optimal loading frequency, which may vary for different setup using Eq. (7) with the pre-stress setting. Based on the above study, geometric patterns with disjoint shapes have a faster separation velocity than a connected shape. Besides, the circle has the

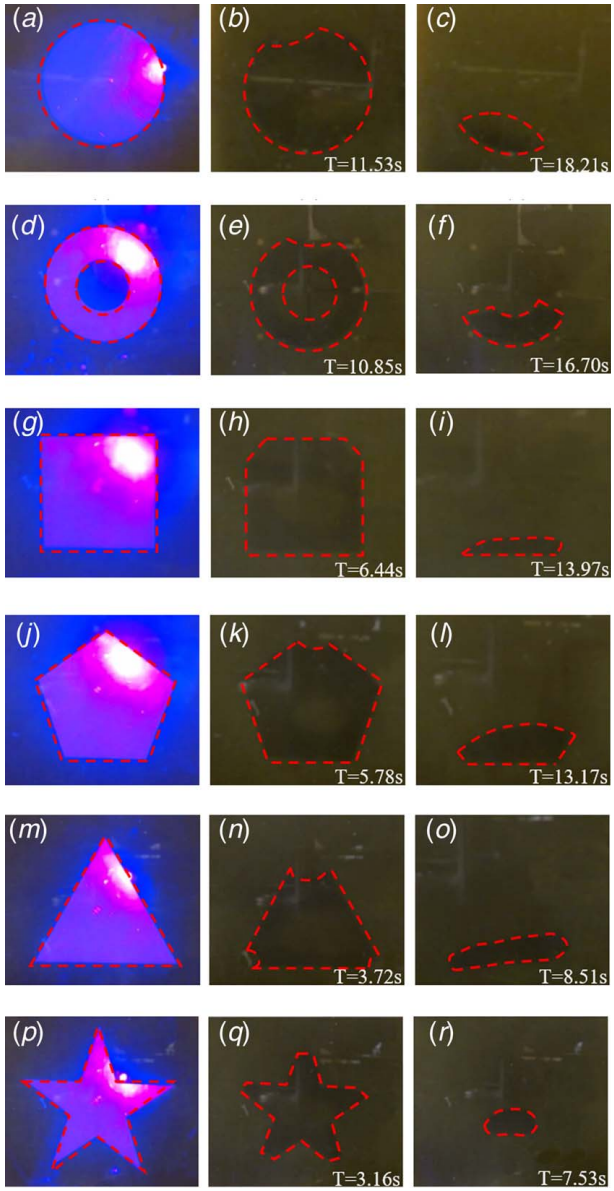

Fig. 12 Crack initiation and propagation for fabricated different shapes, including (*a–c*) circle, (*d–f*) ring, (*g–i*) square, (*j–l*) pentagon, (*m–o*) triangle, and (*p–r*) pentagram

Table 10 Comparison of separation force between the direct pulling-up method and the VA separation-based method

	Direct pulling-up method (without vibration)			VA separation method	
Area (mm^2)	Pulling-up velocity (mm/s)	Separation force (N)	Separation time (s)	Separation force (N)	Separation time (s)
2189	0.06	118.58	6.82	26.55	6.42
4378	0.03	224.96	17.14	54.57	17.12
6567	0.03	346.72	20.77	103.60	21.57

longest separation time among the six geometric shapes that were tested. Therefore, the algorithm provides a conservative estimation. Similar to the "safety factor" in predicting fatigue life, additional vibration time was pre-defined to guarantee the separation of the part-film interface within the given time. If the max stress amplitude

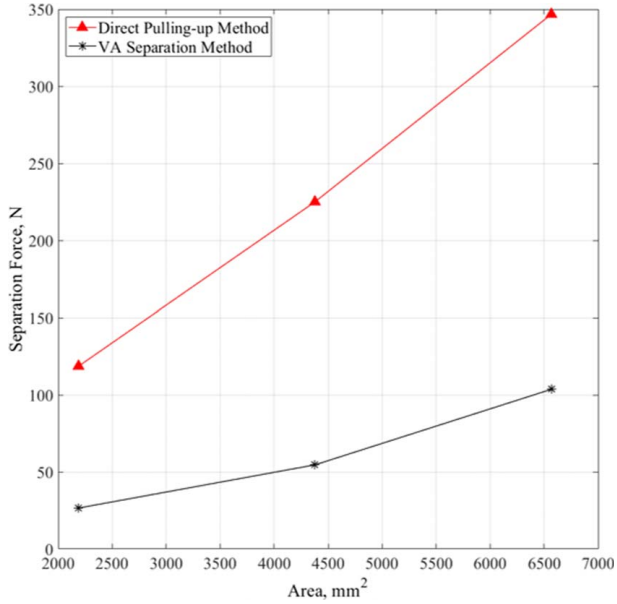

Fig. 13 Comparison of the separation forces of different areas between the direct pulling-up and VA separation-based methods

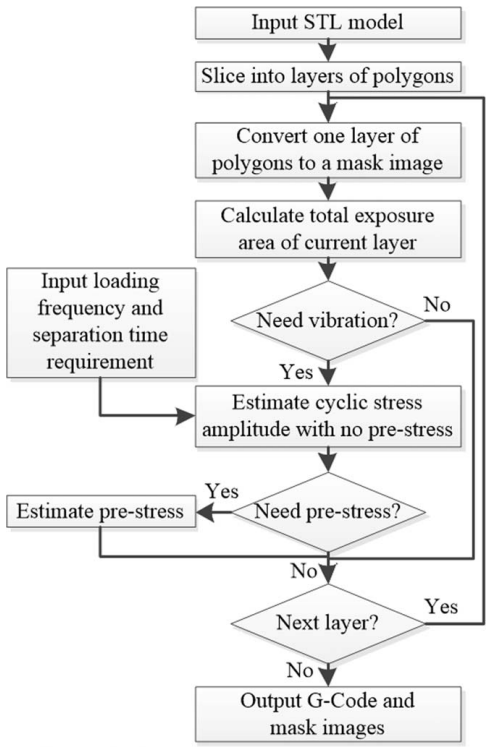

Fig. 14 The algorithm for the VA-SL process

exceeds the capability of the piezoelectric actuator, the pre-stress using Eq. (7) was estimated with the cyclic stress amplitude setting to the max value. The process was repeated until all the two-dimensional (2D) layers of the model have been processed. In the end, the planned mask images and the corresponding G-Code were generated for the given model.

An example of an hourglass was used to demonstrate the effectiveness of our algorithm. In the test case, the required separation time was set to be 30 s, among which 10 s was the additional vibration time. The loading frequency was 500 Hz. The max cyclic loading force was set to 19.5 N. If the circle diameter is smaller

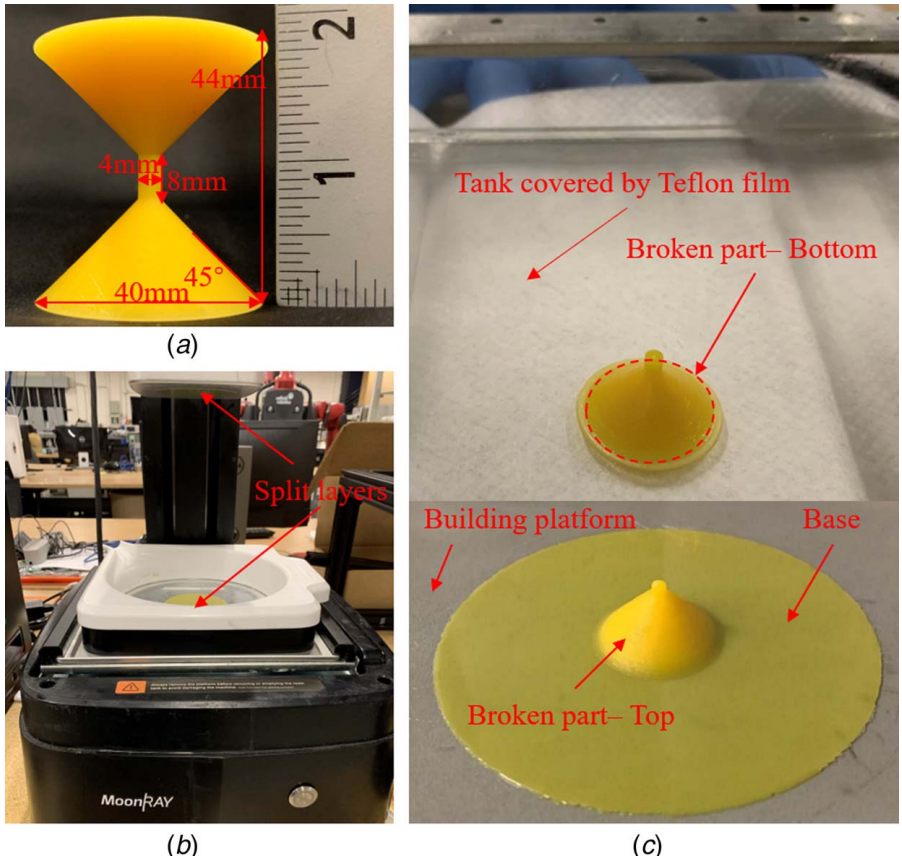

Fig. 15 Printing result of the same hourglass using different separation methods: (*a*) finished part using the VA separation method, (*b*) failed fabrication result using the tilting separation method, and (*c*) failed fabrication result using the direct pulling-up separation method

than 10 mm, the direct pulling-up separation method was used. Using the VA separation method, the hourglass was successfully printed (Fig. 15(*a*)). For the direct pulling-up separation method, the pulling up velocity is 0.5 mm/s. However, the hourglass broke at the neck, which was the weakest portion of the model, and the built layers split into two portions (Fig. 15(*c*)-bottom). One portion was still connected with the building platform, while the other attached to the resin vat surface (Fig. 15(*c*)-top). The dashed circle indicated the layer when the split happened. The same part was also tested on a commercial 3D printer MoonRay (SprintRay, Los Angeles, CA), which adopted a tilting mechanism. However, the splitting of the two neighboring layers was also observed in the printing result due to the large separation force (Fig. 15(*b*)).

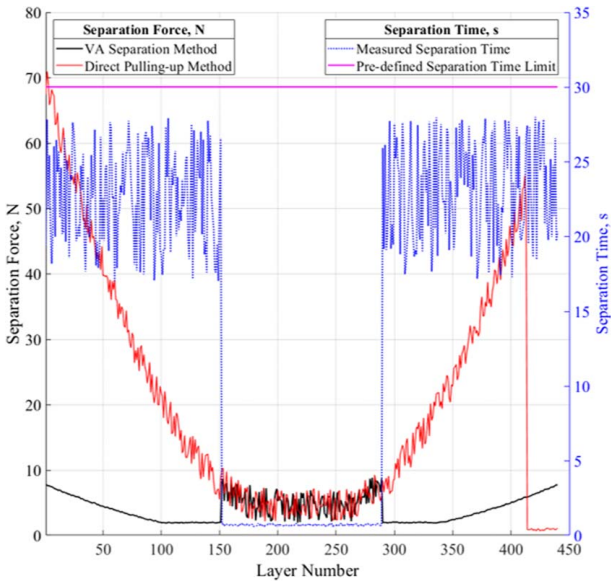

Fig. 16 The measured separation force (left) and the measured separation time (right) of each layer in the hourglass test model using the direct pulling-up and VA separation-based methods

The measured separation force and separation time of each layer are plotted in Fig. 16. Although the separation time was shorter for the direct pulling-up method, the related separation force was much larger. During the fabrication of the second cone of the hourglass, the separation force increased linearly with the increase of the layer area and finally leads to brittle fracture at layer 413. In comparison, the peak force of the VA separation-based method also varied synchronously with the area of each layer; however, the peak force was much smaller than the one recorded in the direct pulling-up method. The comparison of the pre-defined separation time limit and the measured separation time has verified the developed process model to estimate the separation time meets the process planning requirement of the constrain-surface-based SL for large building areas.

6 Conclusion

A vibration-assisted separation method based on the piezo-drive design has been presented for the constrained-surface-based SL process. The influence of various process parameters, including layer area size, geometric shape, and cyclic loading parameters on the vibration-assisted separation method has been studied based

on the mechanics of fatigue fracture. A stress-based model was utilized to estimate the separation time and separation peak force. Accordingly, an algorithm to adjust the process parameters has been developed for the VA separation-based SL process. The experiments based on several designed test cases were performed to demonstrate the effectiveness of the developed prototype system. The comparison between the direct pulling-up separation with and without the vibration-assisted method has verified the VA assisted separation mechanism can significantly reduce the peak separation force in the constrained-surface-based SL process for layers with large cross-sectional areas.

Acknowledgment

This work was partially supported by the National Science Foundation (NSF) 1812675.

Conflict of Interest

There are no conflicts of interest.

Data Availability Statement

The datasets generated and supporting the findings of this article are obtainable from the corresponding author upon reasonable request. The authors attest that all data for this study are included in the paper.

References

[1] Yang, Y., Song, X., Li, X., Chen, Z., Zhou, C., Zhou, Q., and Chen, Y., 2018, "Recent Progress in Biomimetic Additive Manufacturing Technology: From Materials to Functional Structures," Adv. Mater., **30**(36), p. 1706539.
[2] Leung, Y., Kwok, T., Li, X., Yang, Y., Wang, C. C. L., and Chen, Y., 2019, "Challenges and Status on Design and Computation for Emerging Additive Manufacturing Technologies," ASME J. Comput. Inf. Sci. Eng., **19**(2), p. 021013.
[3] Zhou, C., and Chen, Y., 2012, "Additive Manufacturing Based on Optimized Mask Video Projection for Improved Accuracy and Resolution," J. Manuf. Process., **14**(2), pp. 107–118.
[4] Li, Y., Mao, H., Hu, P., Hermes, M., Lim, H., Yoon, J., Luhar, M., Chen, Y., and Wu, W., 2019, "Bio-inspired Functional Surfaces Enabled by Multiscale Stereolithography," Adv. Mater. Technol., **4**(5), p. 1800638.
[5] Pan, Y., and Chen, Y., 2016, "Meniscus Process Optimization for Smooth Surface Fabrication in Stereolithography," Addit. Manuf., **12**, pp. 321–333.
[6] Gritsenko, D., Yazdi, A. A., Lin, Y., Hovorka, V., Pan, Y., and Xu, J., 2017, "On Characterization of Separation Force for Resin Replenishment Enhancement in 3D Printing," Addit. Manuf., **17**, pp. 151–156.
[7] Mao, H., Zhou, C., and Chen, Y., 2016, "LISA: Linear Immersed Sweeping Accumulation," J. Manuf. Process., **24**, pp. 406–415.
[8] Pan, Y., He, H., Xu, J., and Feinerman, A., 2017, "Study of Separation Force in Constrained Surface Projection Stereolithography," Rapid Prototyp. J., **23**(2), pp. 353–361.
[9] Li, X., and Chen, Y., 2017, "Micro-scale Feature Fabrication Using Immersed Surface Accumulation," J. Manuf. Process., **28**, pp. 531–540.
[10] Song, X., Zhang, Z., Chen, Z., and Chen, Y., 2016, "Porous Structure Fabrication Using a Stereolithography-Based Sugar Foaming Method," ASME J. Manuf. Sci. Eng., **139**(3), p. 031015.
[11] Li, X., Mao, H., Pan, Y., and Chen, Y., 2019, "Mask Video Projection Based Stereolithography With Continuous Resin Flow to Build Digital Models in Minutes," ASME J. Manuf. Sci. Eng., **141**(8), p. 081007.
[12] Pan, Y., Zhou, C., and Chen, Y., 2012, "A Fast Mask Projection Stereolithography Process for Fabricating Digital Models in Minutes," ASME J. Manuf. Sci. Eng., **134**(5), p. 051011.
[13] Jin, J., Yang, J., Mao, H., and Chen, Y., 2018, "A Vibration-Assisted Method to Reduce Separation Force for Stereolithography," J. Manuf. Process., **34**, pp. 793–801.
[14] Zhou, C., Chen, Y., Yang, Z., and Khoshnevis, B., 2013, "Digital Material Fabrication Using Mask-Image-Projection-Based Stereolithography," Rapid Prototyp. J., **19**(3), pp. 153–165.
[15] Liravi, F., Das, S., and Zhou, C., 2014, "Separation Force Analysis Based on Cohesive Delamination Model for Bottom-up Stereolithography Using Finite Element Analysis," 25th Annual International Solid Freeform Fabrication Symposium, Austin, TX, Aug. 4–6.
[16] Huang, Y. M., and Jiang, C. P., 2005, "On-line Force Monitoring of Platform Ascending Rapid Prototyping System," J. Mater. Process. Technol., **159**(2), pp. 257–264.
[17] Ye, H., Venketeswaran, A., Das, S., and Zhou, C., 2017, "Investigation of Separation Force for Constrained-Surface Stereolithography Process From Mechanics Perspective," Rapid Prototyp. J., **23**(4), pp. 696–710.
[18] Dendukuri, D., Pregibon, D. C., Collins, J., Hatton, T. A., and Doyle, P. S., 2006, "Continuous-Flow Lithography for High-Throughput Microparticle Synthesis," Nat. Mater., **5**(5), pp. 365–369.
[19] Tumbleston, J. R., Shirvanyants, D., Ermoshkin, N., Janusziewicz, R., Johnson, A. R., Kelly, D., Chen, K., Pinschmidt, R., Rolland, J. P., Ermoshkin, A., and Samulski, E. T., 2015, "Continuous Liquid Interface Production of 3D Objects," Science, **347**(6228), pp. 1349–1352.
[20] Wang, J. C., Ruilova, M., and Lin, Y. H., 2017, "The Development of an Active Separation Method for Bottom-Up Stereolithography System," 2017 IEEE/SICE International Symposium on System Integration (SII), Taipei, Taiwan, Dec. 11–14, IEEE, pp. 108–114.
[21] Yang, S., and Evans, J. R., 2003, "Computer Control of Powder Flow for Solid Freeforming by Acoustic Modulation," Powder Technol., **133**(1–3), pp. 251–254.
[22] Yang, S., Mohebi, M. M., and Evans, J. R. G., 2008, "A Novel Solid Freeforming Method Using Simultaneous Part and Mould Construction," Rapid Prototyp. J., **14**(1), pp. 35–43.
[23] White, D., 2003, Ultrasonic Object Consolidation, Solidica Inc., U.S. Patent 6,519,500.
[24] Sachs, E. M., 2000, Powder Dispensing Apparatus Using Vibration, Massachusetts Institute of Technology, U.S. Patent 6,036,777.
[25] Cong, W., and Ning, F., 2017, "A Fundamental Investigation on Ultrasonic Vibration-Assisted Laser Engineered Net Shaping of Stainless Steel," Int. J. Mach. Tools Manuf., **121**, pp. 61–69.
[26] Kovalenko, I., Garan, M., Shynkarenko, A., Zelený, P., and Šafka, J., 2015, "Examining the relationship between forces during stereolithography 3D printing and geometric parameters of the model," 2015 International Conference on Mechanical Engineering and Electrical Systems, Singapore, Dec. 16–18.
[27] Liravi, F., Das, S., and Zhou, C., 2015, "Separation Force Analysis and Prediction Based on Cohesive Element Model for Constrained-Surface Stereolithography Processes," Comput.-Aided Des., **69**, pp. 134–142.
[28] Wu, X., Lian, Q., Li, D., and Jin, Z., 2017, "Tilting Separation Analysis of Bottom-Up Mask Projection Stereolithography Based on Cohesive Zone Model," J. Mater. Process. Technol., **243**, pp. 184–196.
[29] Dowling, N. E., 2012, *Mechanical Behavior of Materials: Engineering Methods for Deformation, Fracture, and Fatigue*, Pearson, Boston, MA.
[30] Pascoe, J. A., Alderliesten, R. C., and Benedictus, R., 2013, "Methods for the Prediction of Fatigue Delamination Growth in Composites and Adhesive Bonds —A Critical Review," Eng. Fract. Mech., **112**, pp. 72–96.
[31] Duggan, T. V., and Byrne, J., 1977, *Fatigue as a Design Criterion*, Macmillan International Higher Education, London, UK.
[32] Schwalbe, K. H., 1974, "Comparison of Several Fatigue Crack Propagation Laws With Experimental Results," Eng. Fract. Mech., **6**(2), pp. 325–341.
[33] Walker, K., Pendleberry, S., and McElwee, R., 1970, *Effects of Environment and Complex Load History on Fatigue Life*, ASTM International, Philadelphia, PA.
[34] Xin, Q., 2013, *Diesel Engine System Design*, Woodhead Publishing Limited, Sawston, Cambridge, UK, pp. 113–202.
[35] Lin, Y. S., and Yang, C. J., 2019, "Spring Assisting Mechanism for Enhancing the Separation Performance of Digital Light Process 3D Printers," IEEE Access, **7**, pp. 71718–71729.
[36] Bae, K. H., and Lee, S. B., 2011, "The Effect of Specimen Geometry on the Low Cycle Fatigue Life of Metallic Materials," Mater. High Temp., **28**(1), pp. 33–39.